Journal of Structural Biology 189 (2015) 28–36

Contents lists available at ScienceDirect

Journal of Structural Biology

journal homepage: www.elsevier.com/locate/yjsbi

# Layered growth of crayfish gastrolith: About the stability of amorphous calcium carbonate and role of additives

Wouter J.E.M. Habraken [a,*], Admir Masic [a], Luca Bertinetti [a], Ali Al-Sawalmih [b], Lilah Glazer [c], Shmuel Bentov [c], Peter Fratzl [a], Amir Sagi [d], Barbara Aichmayer [a], Amir Berman [e]

[a] Max Planck Institute of Colloids and Interfaces, Department of Biomaterials, 14424 Potsdam, Germany
[b] Marine Science Station (MSS), The University of Jordan/Aqaba Campus, 77110 Aqaba, Jordan
[c] Life Sciences Dept., Ben-Gurion University of the Negev, 84105 Beer-Sheva, Israel
[d] Life Sciences Dept. and the National Institute for Biotechnology in the Negev, Ben-Gurion University, 84105 Beer-Sheva, Israel
[e] Biotechnology Engineering Dept., Ben-Gurion University of the Negev, 84105 Beer Sheva, Israel

ARTICLE INFO

*Article history:*
Received 12 September 2014
Received in revised form 17 November 2014
Accepted 18 November 2014
Available online 26 November 2014

*Keywords:*
Amorphous calcium carbonate
Crayfish
Gastrolith
Hierarchical organization
Stabilization

ABSTRACT

Previous studies on pre-molt gastroliths have shown a typical onion-like morphology of layers of amorphous mineral (mostly calcium carbonate) and chitin, resulting from the continuous deposition and densification of amorphous mineral spheres on a chitin-matrix during time. To investigate the consequences of this layered growth on the local structure and composition of the gastrolith, we performed spatially-resolved Raman, X-ray and SEM–EDS analysis on complete pre-molt gastrolith cross-sections. Results show that especially the abundance of inorganic phosphate, phosphoenolpyruvate (PEP)/citrate and proteins is not uniform throughout the organ but changes from layer to layer. Based on these results we can conclude that ACC stabilization in the gastrolith takes place by more than one compound and not by only one of these additives.



## 1. Introduction

Only recently it was discovered that Nature uses amorphous materials as precursor phases preceding the formation of elaborate crystalline structures and tissues, like the spicules of sea-urchins (Beniash et al., 1997; Politi et al., 2004), zebrafish bone (Mahamid et al., 2011) and in many more cases (Addadi et al., 2003). In those examples the formation of an eventual crystalline material (i.e. calcite, aragonite, or apatite) proceeds via an amorphous precursor state that under *in vitro* conditions is often only present as a kinetically stabilized intermediate (Sawada, 1997).

In contrast to pure synthetic amorphous calcium carbonate or phosphate, in biological samples, the amorphous phase can also be much more stable against thermodynamic pressure, forming functional end-products like the crayfish exoskeleton (Bentov et al., 2012) without transforming into a crystalline polymorph. This phenomenon is speculated to result from the presence of molecular agents that stabilize the amorphous phase and delay crystal formation. From studies on skeletons of marine organisms a wide scale of such stabilizing agents is proposed. Examples are highly charged and/or phosphorylated proteins, small organic molecules, foreign ions (especially $Mg^{2+}$ (Politi et al., 2010)) and specialized macromolecules (Aizenberg et al., 1996). Studies on synthetically grown calcium carbonate or calcium phosphate under physiological conditions have shown that highly charged polymers like poly(aspartic acid) are able to stabilize a so-called Polymer-Induced Liquid Precursor (PILP) phase (Olszta et al., 2007). PILP represents a highly hydrated non-crystalline mineral phase, which is believed to resemble amorphous precursors in many biological systems. Additionally, the influence of (small) organic molecules as well as foreign ions on *in vitro* calcium carbonate/calcium phosphate growth has been studied since the 1970's. These studies show that it is possible to delay the reaction kinetics (and thereby increase the stability of the amorphous phase) quite radically by only introducing a small amount of mostly acidic agents or polyvalent ions (f.e. pyrophosphate, casein, $Mg^{2+}$, $SO_4^{2-}$) (Termine et al., 1970; Ihli et al., 2013). Non-acidic agents or monovalent ions (f.e. $Na^+$, gelatin), in general, leave the reaction unaffected.

In this study we investigated the stable amorphous calcium carbonate (ACC) in the crayfish temporary mineral storage, the gastrolith. Crayfish need a large amount of mineral during the molting cycle. Therefore, some species of fresh-water crayfish have a specialized storage-the gastrolith, first described by Huxley

* Corresponding author.
*E-mail address:* wouter.habraken@mpikg.mpg.de (W.J.E.M. Habraken).

http://dx.doi.org/10.1016/j.jsb.2014.11.003
1047-8477/

(1880). Gastroliths are located between the endocuticle and epidermis of the gastrolith disks (Travis, 1963), organs dedicated to the production of the gastrolith, which are situated on both sides of the stomach. The growth of the gastroliths involves first the deposition of a poorly ordered lamellar α-chitin matrix, with orthogonally directed shorter chitin fibers. Accordingly, the amorphous mineral attaches on this matrix as nanometer-sized spheres (Travis, 1963). In this process, both the chitin matrix and the mineral particles are secreted by the epidermal cells of the gastrolith disk. As the gastrolith matures, new mineral is deposited on the external layer, while the earlier deposited mineral densifies into macroscopic columnar structures, directed parallel to the growth direction. In time, the composite of the lamellar chitin and the mineral forms an ordered structure of concentric layers (Travis, 1963), which is finally resorbed through collapse of the tissue into the crayfish stomach during ecdysis (Shechter et al., 2008a).

It is postulated that certain proteins found in the crayfish gastroliths take part in the mineralization of the chitin scaffold by playing different roles in modulating mineralization (i.e. stabilizing ACC) and attaching the chitin to the mineral. These proteins include the gastrolith matrix protein (GAMP) (Takagi et al., 2000), gastrolith protein 65 + 75 (GAP65 + GAP75) (Shechter et al., 2008b; Glazer and Sagi, 2012), CqCDA1 (Yudkovski et al., 2010) and gastrolith protein 10 (GAP10) (Glazer et al., 2010)). Conversely, recent ss-NMR studies (Sato et al., 2011; Akiva-Tal et al., 2011) indicate that small organic molecules like phosphoenolpyruvate (PEP) and citrate but most of all inorganic phosphate (Akiva-Tal et al., 2011), present in gastroliths up to an average of maximally 18 wt%, are the most likely candidates to stabilize ACC in the gastrolith. Note that unlike $Mg^{2+}$, inorganic phosphate is not a substitutional impurity in any crystalline calcium carbonate. Furthermore, the chemical environment of the phosphate elucidated in ss-NMR (Akiva-Tal et al., 2011) indicates that it is well dispersed inside the ACC structure. These observations, however, do not rule out that a combination of several factors (proteins, inorganic phosphate, small organic molecules) could act cooperatively to enhance the stability of gastrolithic ACC. Additionally, taking into account the prospected layer-by-layer deposition, local differences in structure and composition, as indicated in previous work (Akiva-Tal et al., 2011; Bentov et al., 2010) could provide vital clues for the stabilization mechanism of ACC.

In order to better understand the thermodynamic stability and structure of gastrolith mineral in relationship to its biological formation history and purpose, in this study we performed spatially-resolved analysis on whole pre-molt gastrolith slices or cross-sections. To obtain a complete chemical, structural and morphological description of the gastrolith at different length scales, Raman spectroscopy and synchrotron small-and wide angle X-ray scattering (SAXS/WAXS) were combined with light microscopy imaging, high-resolution scanning electron microscopy (SEM) and EDS analysis. Results show that the structure as well as the content of inorganic phosphate, chitin, protein and citrate or PEP show layer-to-layer variations. Such a distribution indicates that the remarkable stability of the ACC is not governed by only one of these compounds, but that depending on the specific layer investigated, different stabilizing agents are involved.

## 2. Materials and methods

### 2.1. Preparation of the gastrolith cross-sections

Pre-molt gastroliths were extracted from the animals reared at BGU, and cleaned using distilled water. For SAXS/WAXS and light microscopy, samples were embedded in epoxy-resin (EPOFIX™) and sectioned using a diamond knife producing 0.7–1.0 mm thick slides, concomitantly cooled by ethylene glycol to prevent crystallization. Additionally, for chemical and structural characterization by Raman and SEM, gastrolith cross-sections were prepared by cutting the gastrolith with a scalpel blade while frozen by liquid nitrogen.

### 2.2. Light microscopy

Light microscopy images of gastrolith slides were taken by a Leica DM RXA2 microscope at a magnification of 2.5×. For visualization of the total gastrolith, images of different (overlapping) regions were combined afterwards using Microsoft Powerpoint™.

### 2.3. Scanning electron microscopy + energy dispersive X-ray spectroscopy

Scanning electron micrographs were obtained with a Jeol JSM7500F. Images were acquired at an acceleration voltage of 2 kV and a working distance (WD) of about 8 mm, using a through-the-lens secondary electron detector. The freshly exposed surfaces of the samples were coated with a layer of 2–3 nm of Pt prior to the investigations. Analytical information was obtained at 15 kV and at the same WD used for imaging through an Oxford Inca Energy Dispersive Spectroscopy System (EDS) using an X-Max™ silicon drift detector (spatial resolution ~ 2 μm). Using this equipment we were able to detect less than 2 mol% of P. Particle size measurements on SEM-images were performed using ImageJ™ software.

### 2.4. Raman spectroscopy

Raman spectra were collected with a confocal Raman microscope (α300; WITec) equipped with a Nikon objective (20×) a laser excitation wavelength of 532 nm and a spatial resolution of ~700 nm. Spectra were acquired with a CCD camera (DV401-BV; Andor) behind a spectrometer (UHTS 300; WITec) with a spectral resolution of 3 $cm^{-1}$. For the line scans, light microscopy images and corresponding spectra were taken every 50 μm. Data analysis (subtracting background, fitting area beneath specificated peaks) was done using WITec™ software. A rough estimation of P levels by Raman was done by comparison of the area of the $\nu_1$ of $PO_4^{3-}$ (~960 $cm^{-1}$) with the $\nu_1$ of $CO_3^{2-}$ (~1080 $cm^{-1}$). As a standard, synthetic P-containing ACC (ACCP) was prepared by adding a concentrated $CaCl_2$ solution to a 98:2 mixture of $Na_2CO_3$ and $Na_2HPO_4$. From inductively coupled plasma optical emission spectrometry (ICP–OES) analysis, 1.6 mol% of P was measured inside the P-ACC standard.

### 2.5. Synchrotron small- and wide angle X-ray scattering and X-ray diffraction measurements

Small and wide-angle X-ray scattering (SAXS + WAXS) measurements on embedded gastrolith slices were performed at the μ-Spot beamline (BESSY II storage ring, Helmholtz-Zentrum Berlin) (Paris et al., 2007) using a multilayer monochromator and spot size of 100 μm. Radially averaged scattering patterns were obtained using FIT2D™ software and corrected for sample thickness (transmission), intensity of X-ray beam and background. For quantitative peak area determination of the WAXS patterns, the two amorphous signals of ACC (AMO1 at $q \cong 22$ $nm^{-1}$, AMO2 at $q \cong 32$ $nm^{-1}$) and the α-chitin (1 1 0) at $q \cong 14$ $nm^{-1}$ were fitted by gaussian curves using Origin™ Software.

## 3. Results

### 3.1. Structural differences due to layered growth of gastrolith

The epoxy-embedded slices, cut in two different modes (parallel to the growth direction (Fig. 1A and C) and perpendicular to this (Fig. 1B), see also inset Fig. 1), are translucent to transmission light microscopy, revealing concentric rings with lighter and darker regions starting from the earlier deposited innermost layers (i) to the later deposited external (e) parts. An additional feature is the presence of columns orthogonal to these concentric rings (see arrows in Fig. 1A and C) (Travis, 1963). As a consequence, where the slice is completely perpendicular to the growth direction (inner part of Fig. 1B), the layered structure is not apparent and the columnar organization appears as elongated dots. These structural features can be seen independent of the size of the gastrolith (compare Fig. 1A with Fig. 1C), indicating a similar structural organization between gastroliths extracted from crayfish of different ages.

As the slice thickness is uniform, changes in opacity may be caused by the different densities of the mineral layers. It might also be due to a submicron-sized porosity within the sample that changes from layer to layer, or due to intermittent deposition of organic compounds absorbing in the visible light range (390–700 nm). These changes can be quite dramatic as radial integration of the indicated region in Fig. 1A shows, causing 4-fold variation (10–40 AU) in scattered light intensity (Fig. 1D). The chemical variation in P, also shown in Fig. 1D, will be described later on.

To investigate the source of this opacity, high-resolution SEM was performed on a non-embedded gastrolith cross-section that was cut after quenching in liquid nitrogen. As amorphous calcium carbonate is ductile, the cutting process itself interferes with the correct structural characterization, as small pores/structures get smeared at the surface. By quenching the material in liquid nitrogen, the mineral hardens thereby retaining more of its original structural features. Corresponding to the structures observed in transmission light microscopy, initial SEM investigation of the whole cross-section (Fig. 2A) shows radially distributed cracks in the middle and oldest layers of the gastrolith, as well as smaller orthogonal cracks. Though possibly created by the drying or freezing processes, these cracks indicate mechanically weak regions or materials with different thermal expansion coefficients inside the gastrolith structure. The cracks also partially follow the positions of the darker layers in the middle of the gastrolith in transmission light microscopy images (see Fig. 2D). Here they seem to be associated with the interface between the darker layers and surrounding transparent regions, as will be even clearer by chemical analysis discussed in the following paragraphs (see Fig. 2B). As the dimensions of the cracks are much smaller than the darker regions in light microscopy, and only a part of these regions are associated with cracks in SEM, this excludes the cracks as being the cause for this difference in opacity.

At a higher magnification (Figs. 3 and 4), except for the innermost layers, through the whole gastrolith sub-micron-sized spherical features are observed. As expected from literature (Travis,

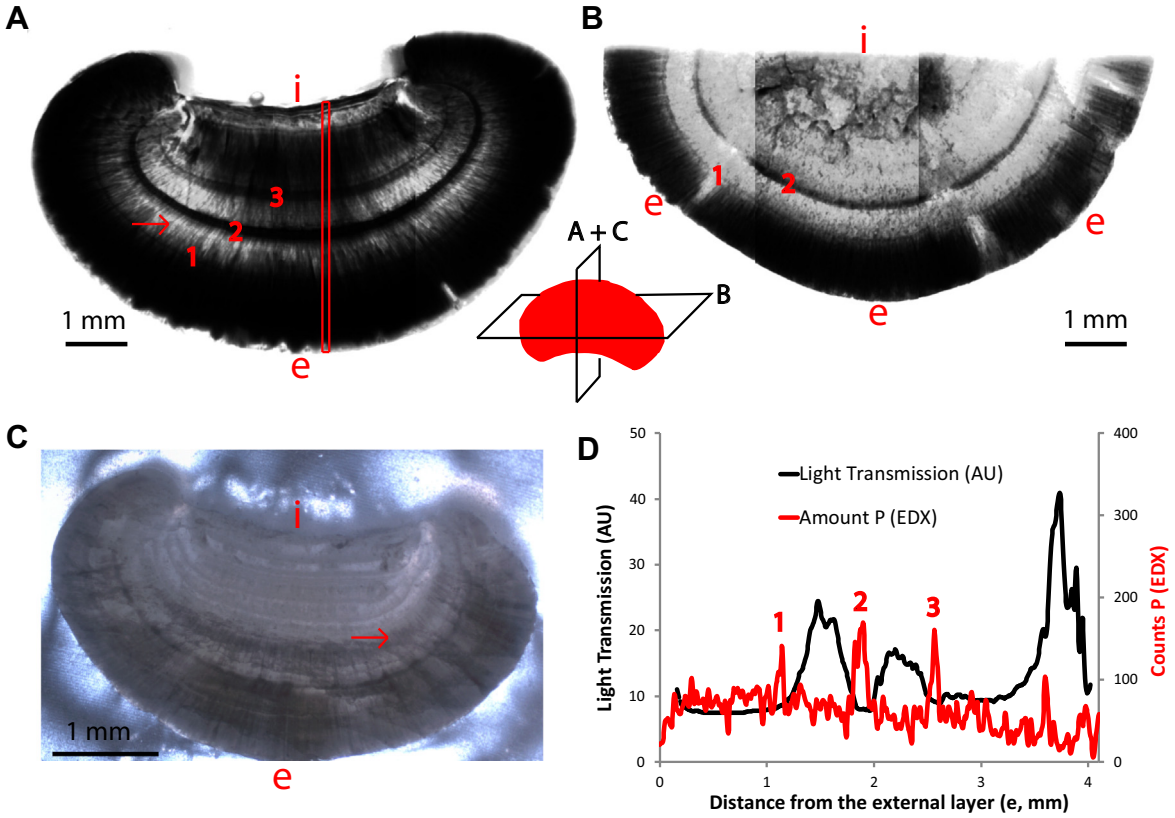


**Fig.1.** Transmission light microscopy on gastrolith sections, (A + B) Large gastrolith cut in two different modes (see also inset): (A) parallel to the growth direction showing distinct growth lines from the earlier deposited innermost layers (indicated by i) to the later deposited external parts (indicated by e), (B) perpendicular to A, due to the curved shape especially at the external parts of the gastrolith the growth lines are also visible here. (C) A smaller gastrolith (size ~ 2× smaller), cut parallel to the growth direction, (D) Light transmission (in Arbitrary Units) and relative amount of P as measured by EDS as a function of the distance from the external layer (e) after integrating the square area as indicated in (A). The light transmission graph is cut at the outer 100 μm on both sides due to interference with embedding material. Peaks 1, 2 and 3 correspond to regions with low transmission as indicated in A and B. Arrows indicate the stacking of columnar features.

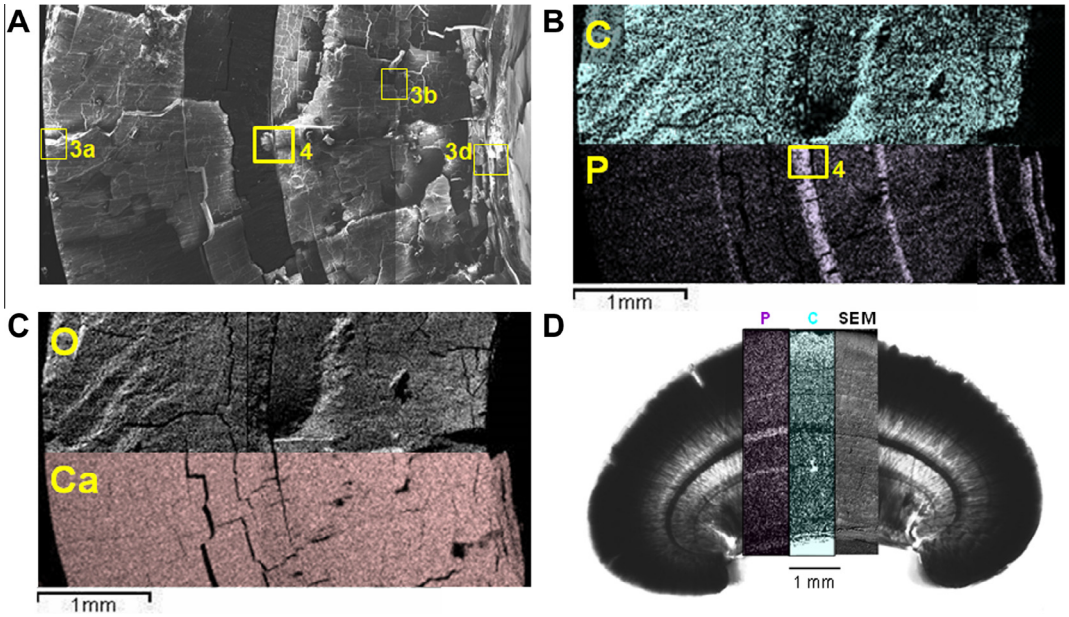


**Fig.2.** Scanning electron microscopy and EDS maps of a gastrolith cross-section. (A) Scanning electron microscopy, (B) C and P maps, (C) Ca and O maps, (D) overlay of a transmission light microscopy image with SEM and P + C maps. The squares in A and B indicate the positions of Figs. 3 and 4.

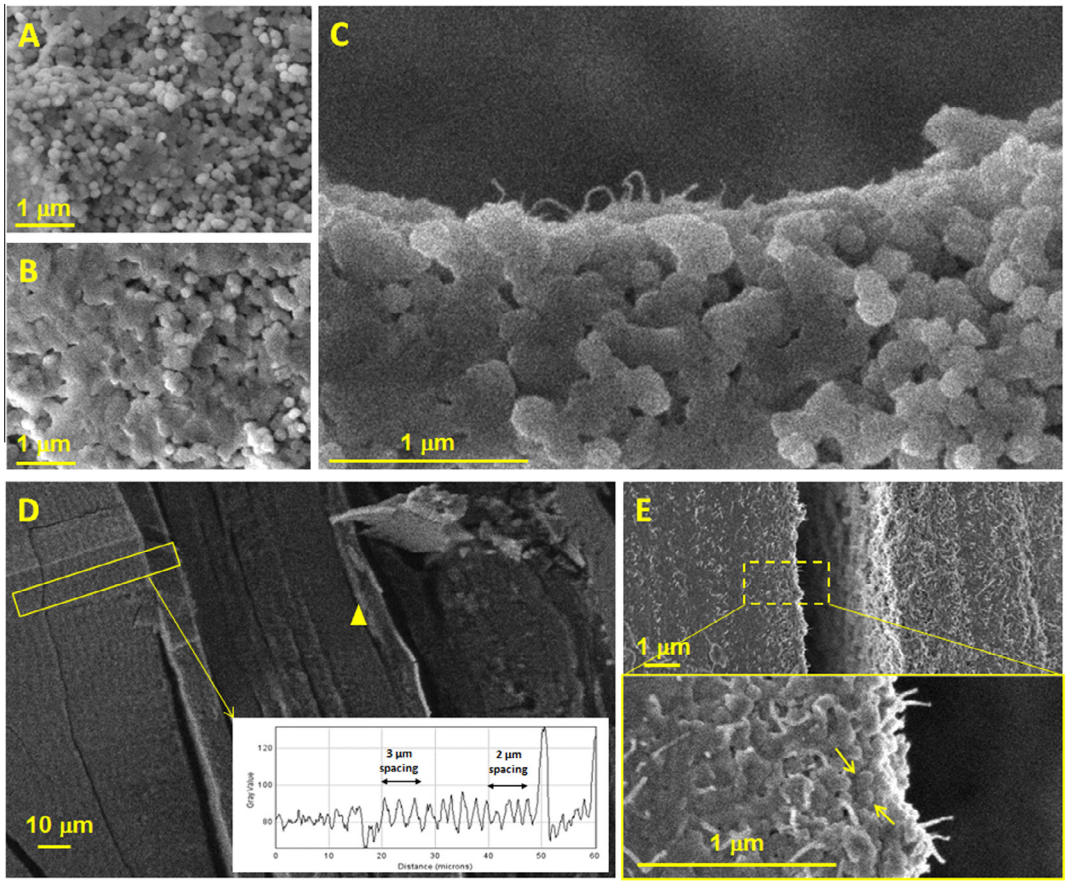


**Fig.3.** High-resolution SEM imaging (A) loose packing of spheres (153 ± 20 nm), (B) compaction of spheres (190 ± 27 nm) showing a high degree of agglomeration, (C) single chitin fibers ($d \sim 5$ nm) sticking out of a crack, (D + E) early deposited inner parts showing ordered layers with higher contrast in SEM (D, see inset). These layers contain aligned chitin bundles (E, ~10–20 nm thick), coated by a dense or fine granular mineral (size granules 99 ± 11 nm, see arrows). Size is presented as mean diameter ± standard deviation. The position of the layer visualized in E is indicated by the Δ-sign in D.

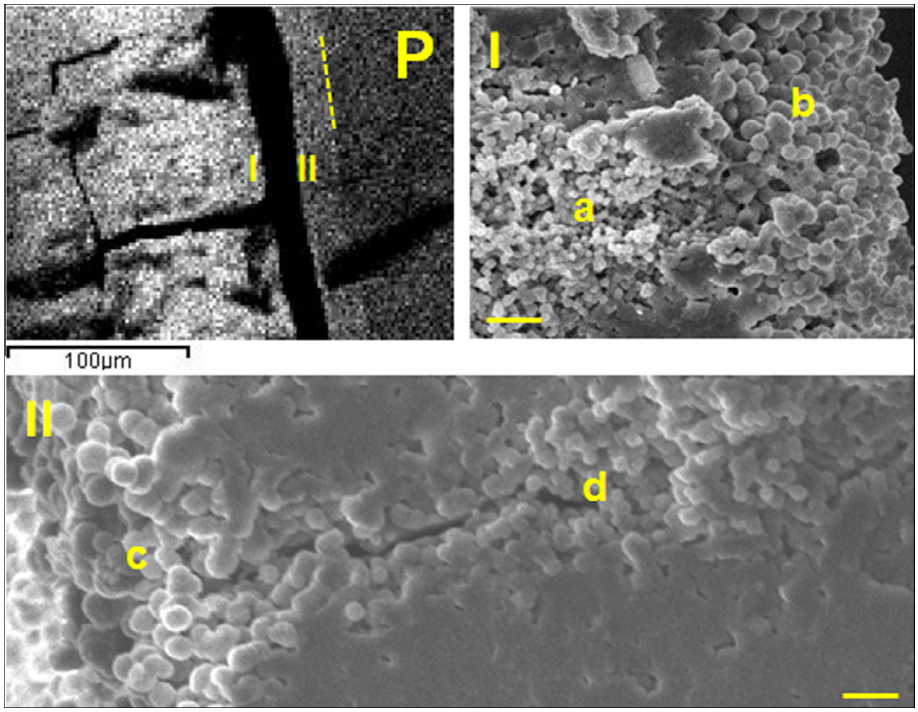


**Fig.4.** Close up of the phosphate rich (I) and phosphate poor (II) regions in the middle of the gastrolith by EDS and high-resolution SEM. (I) and (II) indicate regions left and right of the crack. Size of the spheres in sub-regions a–d: (a) 137 ± 17 nm, (b) 265 ± 49 nm, (c) 437 ± 68 nm and (d) 243 ± 31 nm. Sphere size is presented as mean diameter ± standard deviation. Scale bar in I and II is 1 µm.

1963; Shechter et al., 2008a), in the later deposited external layers of the gastrolith these spheres are more loosely packed and less fused (Fig. 3A) than in earlier deposited inner parts (Fig. 3B), with a sphere-size ranging from 150 nm (Fig. 3A) to 190 nm (Fig. 3B) in most regions. Here, what appears to be loose chitin fibers with a diameter of about 5 nm can be observed around the spheres and sticking out of cracks (Fig. 3C). Also around the cracks in the middle of the gastrolith (Fig. 4), the spheres show an exceptional loose packing and particle sizes ranging from slightly smaller than average (region a: ~140 nm) to exceptionally large spherical particles (b: ~265 nm, c: ~440 nm). The lower amount of interconnections between the large separate spheres could explain why the gastrolith is broken at this position. Additionally, between regions a and b we see a high amount of organic material, containing chitin fibers, which seem to separate both sizes of spheres. Up to this point, comparing the SEM data with the transmission light microscopy images, we can deduce that the light–dark layering is caused by the alternation of loosely to more densely packed or fused submicron sized spheres. Proceeding toward the innermost part of the gastrolith in Fig. 3D we observe multiple, large layers (right) separated from the main body of the gastrolith (left). On a higher scale of hierarchy (Fig. 3E), these separated large layers consist of a finer layering (every ~ 0.5 µm) of mostly 10–20 nm-sized chitin fibers and protein sheets in between a granular amorphous mineral, with average particle size of approximately 100 nm (see arrows Fig. 3E). The increase in size of the chitin fibers with respect to the later deposited external parts possibly indicates that they are covered by mineral or protein.

Also in the main body of the gastrolith (left of Fig. 3D) we observe the alternate layering indicated by the changes in scattered electron intensity, where spacing between the layers is in between 2 and 3 µm (see also inset Fig. 3D). This data indicates a periodic deposition of chitin and mineral, which is much more dense in the early deposited layers, as has been observed before (Travis, 1963). Furthermore, though only observed in embedded

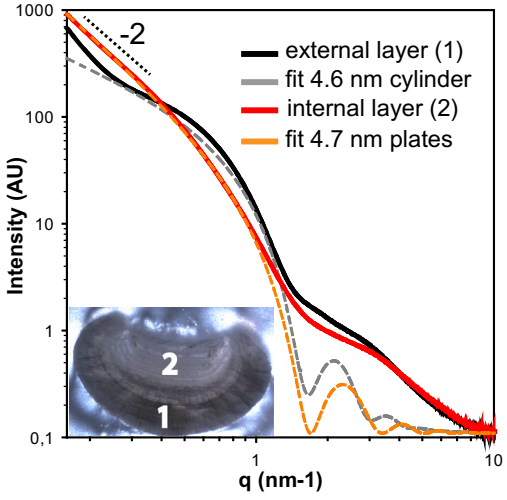


**Fig.5.** SAXS analysis on a small gastrolith. Radially integrated SAXS data from a late deposited external and earlier deposited inner part of the gastrolith (numbers (1 and 2, respectively) are taken at positions shown in inset) fitted with the form factor of 4.6-nm cylinders (i.e. chitin fibers) and 4.7-nm thick plate-like structures (i.e. layers of chitin fibers).

slices of the smaller gastrolith (in Fig. 1C), synchrotron small-angle X-ray scattering (SAXS) at the inner, dense, parts of the sample shows a slope of −2 up to $q = 0.3\ nm^{-1}$ (Fig. 5). Despite the very close packing, a slope of −2 indicates a more plate-like structure (Glatter and Kratky, 1982) and would correspond to such an ordered distribution of thin chitin layers (fitted by plates with a thickness of 4.7 nm), inside a dense calcium carbonate (Fig. 5), under the presumption of a large enough density difference between the chitin and the mineral. Interestingly, the SAXS-pattern of the external layers shows a hump at around $0.9\ nm^{-1}$,

which can be fitted by cylinders with a diameter of 4.6 nm (see Fig. 5). This structure corresponds to the presence of single chitin fibers in these regions, and therefore is in line with our SEM observations.

### 3.2. Compositional changes due to layered growth of gastrolith

To spatially resolve the composition of the gastrolith, first an elemental analysis was performed using Energy dispersive X-ray spectroscopy (EDS). Maps for carbon (C), phosphorous (P), calcium (Ca) and oxygen (O) are given in Fig. 2B and C. Most striking here is the distribution of phosphorous (Fig. 2B), showing distinct maxima in concentration in some radial distributed layers of the gastrolith, which correspond to the darker layers in transmission light microscopy (see also Figs. 1 and 2 D). Together with the loose packing of spherical features in the middle of the gastrolith, where P-content seems to be highest (Fig. 4), this indicates a correlation between the phosphorous content and nanosphere stability against aggregation. However, also the age of the layers seems to play a role here, where in the later deposited external layers the spheres are loosely packed, although here P-contents are very low.

Fig. 4, further, tells us that in the gastrolith there is no direct correlation between sphere size and phosphate content as sizes in the phosphate-rich area (especially a, b and c) range from slightly smaller than average (~140 nm, a) to extremely large particles (~440 nm, c). Finally, the abrupt change in P as seen between region II and the phosphate bulk, indicates a step-wise change in composition, corresponding to the layered deposition of the mineral.

The other EDS-maps (Fig. 2B–D) tell us that the maxima in P seem to correspond to minima in C, whereas Ca and O are more evenly distributed throughout the gastrolith. Such a trend indicates that at these positions there is a high concentration of inorganic phosphate (replacing C by P), whereas the presence of high amounts of phosphorylated proteins or small organic molecules, rather would cause an increase in C and a decrease in $Ca^{2+}$.

To investigate the composition in greater detail, Raman spectroscopy line scans were performed on the same gastrolith cross-sections (Fig. 6A and B). Spectroscopy data are shown in Fig. 6A. Integration of some of the peaks (Fig. 6B) reveals a trend in composition going from the later deposited external layers (spectrum nr. 3) to the earlier deposited inner layers (spectrum nr. 80). Analysis of the Raman spectra suggest that the P-rich regions are in fact containing a predominantly basic inorganic phosphate ($PO_4^{3-}$), as can be derived from the positions of the main signal at 960 $cm^{-1}$ ($\nu_1$ $PO_4^{3-}$), as well as the presence of less intense vibrations at 440 $cm^{-1}$ ($\nu_2$ $PO_4^{3-}$) and 600 $cm^{-1}$ ($\nu_4$ $PO_4^{3-}$) (Fig. 6B and C). Indeed the distribution of the $PO_4^{3-}$ follows very well the P-distribution in EDS, where the most intense signals are coinciding with a decrease in inorganic carbonate, and $PO_4^{3-}$ levels are varying between 1 and 30 mol% (see Table 1). Furthermore, the broadness of the main phosphate (width $\nu_1$ $PO_4^{3-} \sim 30\ cm^{-1}$) and carbonate (width $\nu_1$ $CO_3^{2-} \sim 28\ cm^{-1}$) signals confirms the amorphous nature. This can also be concluded from synchrotron wide-angle X-ray scattering (WAXS) data of the embedded samples (Fig. 7). Here, independent of the position in the gastrolith, all mineral shows a very similar, amorphous diffraction pattern consisting of two broad Gaussian-shaped bands (AMO1 and AMO2) with maxima at around 22 $nm^{-1}$ and 31 $nm^{-1}$. However, after careful fitting the bands with Gaussians we can observe that the position of the fitted peak at 22 $nm^{-1}$ shifts to lower values at the same places in the gastrolith where EDS shows a higher P-concentration (Fig. 7B, left axis and Fig. 7C, right axis). At the same time the ratio in area between AMO2 and AMO1 moves toward lower values (Fig. 7B, right axis). This behavior, where the shape of the WAXS pattern depends on the P-concentration, can be explained by comparing the WAXS patterns of the gastrolith with the WAXS-patterns of synthetically pure ACC and ACP (Inset, Fig. 7A*). Here, both the positions of AMO1 and AMO2 as well as the ratio in area between both peaks are distinctly different between ACC and ACP. For example, the AMO1 of ACP has a maximum (~21.6 $nm^{-1}$) at a lower q than the AMO 1 of ACC (~22.2 $nm^{-1}$). Furthermore, the AMO2 of ACP is much less prominent than the AMO2 of ACC, resulting in an AMO2/AMO1 ratio of ~0.6 for ACP and ~1.2 for ACC. As for the gastrolith, the shifts in the WAXS pattern from a P-poor region to a P-rich region correspond to shifts from a more ACC-like pattern to a more ACP-like pattern, this also indicates that this is caused by the increase of inorganic P inside the sample.

Raman also reveals multiple signals of organic components. Here, chitin signals are most intense in the late external layers of the gastrolith, decreasing stepwise when approaching the earlier deposited inner parts (Fig. 6B). Its trend is similar to signals that can be appointed to aromatic amino acids (phenylalanine, tryptophan, tyrosine) (Fig. 6B and C), which is not surprising as α-chitin fibers in crayfish are described to be coated by these protein residues (Iconomidou et al., 2001). Furthermore, its trend seems to be opposite to the inorganic phosphate, but this does not hold for all samples. Using the WAXS data on the embedded samples, we are able to qualitatively follow the amount of chitin at different positions in the gastrolith by measuring the intensity of the chitin (1 1 0) peak throughout the gastrolith cross-section, and dividing it by the total area of scattering intensity (Fig. 7C). Also from these results we can observe that the gastrolith consists of chitin-rich and chitin-poor regions, but not necessarily increasing in chitin content from the inner to the external regions, or following changes in phosphate concentration.

In the Raman spectrum of the external layers, a small signal at 786 $cm^{-1}$ was observed (Fig. 6A). This signal can be assigned to either the main peak of PEP and/or citrate (De Gelder et al., 2007), both components that were described to be possible candidates for ACC stabilization in gastroliths (Sato et al., 2011; Akiva-Tal et al., 2011). Corresponding to this research (Akiva-Tal et al., 2011), the concentration of PEP and/or citrate seems to be very small; additionally our study shows that their distribution has only limited overlap with inorganic phosphate (Fig. 6B). A signal at 851 $cm^{-1}$ can be assigned to a non-aromatic amino acid like serine. Looking at its trend, and at the trend of the alkyl region between 2880 and 2940 $cm^{-1}$, they seem to coincide completely in the oldest deposited, innermost parts of the gastrolith (see Fig. 6B and C).

## 4. Discussion

When analyzing biological samples like gastroliths, there is a large variation between individual specimens. Therefore, the utmost attention must be taken when drawing general conclusions out of this data, irrespective of the sample size analyzed. However, there is something to be learned from this sample variation itself. As explained in the introduction, the gastrolith is built up by deposition of a chitin matrix and subsequent mineralization of this matrix by spherical mineral particles, which are excreted by neighboring epithelial cells. This process repeats to form successive layers in the structure (Travis, 1963). Whereas the way the gastrolith is formed seems similar throughout the growth process, the composition of the deposited mineral particles changes in different manners. A prime example is the inorganic phosphate content, where depending on the layer investigated, sometimes higher and sometimes lower amounts are present inside the ACC. The reason for this phenomenon could be different; however, while the gastrolith develops in 14 days (Shechter et al., 2008a) growing ~ 500 μm a day, this seems too fast for fluctuations in phosphate availability by a changing diet, or by resorbing different

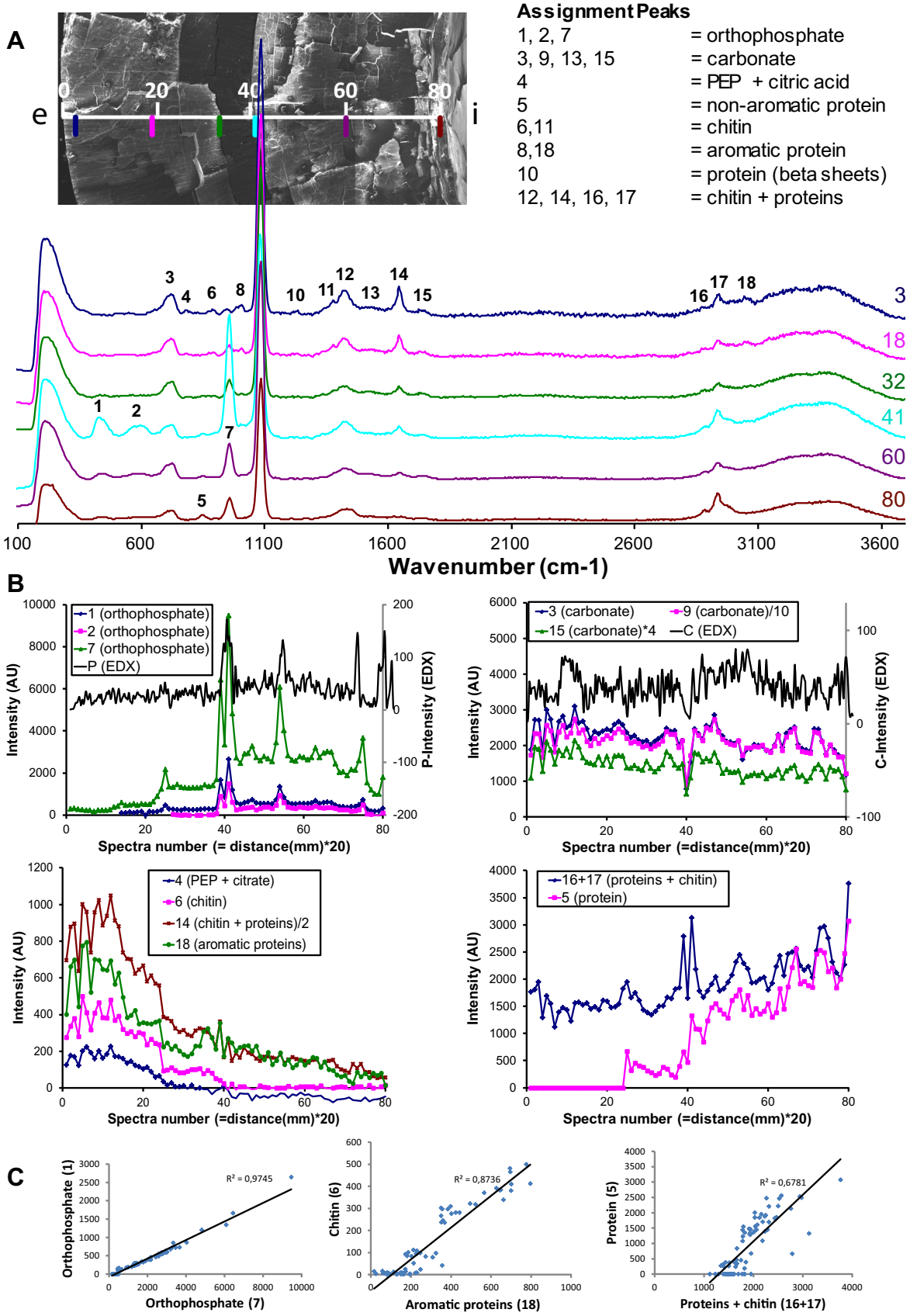


**Fig.6.** Raman-line scans, (A) Raman spectra taken at six different coordinates (3–80) as indicated in the picture (left top) + assignments of the various peaks, (B) Intensity of the Raman peaks as a function of spectra number for orthophosphate and corresponding P-EDS data (left top), carbonate and corresponding C-EDS data (right top), chitin + aromatic protein + PEP/citrate (left bottom) and non-aromatic protein + chitin (right bottom), (C) Statistical correlations between the different Raman Peaks, peak 1 (orthophosphate) vs. peak 7 (orthophosphate) (left), peak 6 (chitin) vs. peak 18 (aromatic protein) (middle) and peak 5 (protein) vs. peaks 16 + 17 (proteins + chitin) (right).

**Table 1**
Estimation of phosphate in sample using Raman area evaluation.

| Sample | Raman area ratio $\nu_1$ $PO_4^{3-}$/($\nu_1$ $CO_3^{2-}$ + $\nu_1$ $PO_4^{3-}$) | Mol% of $PO_4^{3-}$ |
|---|---|---|
| Synthetic ACCP | 0.020 | 1.6 |
| Spectrum nr. 3 (late deposited layers) | 0.012 | 1.0[a] |
| Spectrum nr. 18 | 0.022 | 1.8[a] |
| Spectrum nr. 32 | 0.062 | 5.0[a] |
| Spectrum nr. 41 | 0.354 | 28.6[a] |
| Spectrum nr. 60 | 0.127 | 10.3[a] |
| Spectrum nr. 80 (early deposited layers) | 0.128 | 10.4[a] |

[a] Calculated based on area ratio and ICP data of the synthetic P-containing ACC (ACCP).

parts of the old exoskeleton. As phosphate is found to be a necessary constituent of the crayfish' exoskeleton, used for the production of the enamel-like teeth (Bentov et al., 2012) but also present in the rest of the exoskeleton (Sato et al., 2011), a more sophisticated signaling strategy that controls the amount of phosphate inside the gastrolith could also be an option. However, this might over interpret the role of the gastrolith as it represents only a fraction of the total amount of mineral used for molting (Travis, 1963). Nevertheless, as a result of these compositional changes within a single gastrolith, differences between individual gastroliths may be huge. This is especially true when taking into account differences caused by the age of the crayfish (molt cycles are much shorter with young crayfish), and its diet. What is most remarkable here is that despite of this huge variation, the mineral inside the gastrolith in all cases is a very stable amorphous mineral. Other than concluding that, obviously, a wide range of phosphate concentrations lead to a similar stability, our Raman results show that even without a detectable amount of phosphate in the external layers of the gastrolith, there still is a stable amorphous calcium carbonate. However, here we do see evidence for the presence of phosphoenolpyruvate (PEP) and/or citrate, also discussed to be stabilizing agents for ACC in gastroliths (Sato et al., 2011; Akiva-Tal et al., 2011). This result indicates that from layer to layer the amorphous calcium carbonate can be stabilized using a different stabilizing agent. Furthermore, it is quite understandable that 100–200 nm-sized granules do not crystallize due to a combination of size restriction and presence of phosphate or citrate/PEP. However, in the gastrolith we observe that even at places where these granules are agglomerated into μm-sized prismatic features, the mineral is still amorphous. In these, predominantly early deposited inner regions, we do see a dense layering of chitin fibers/protein by SEM and SAXS. Such a structure does not only

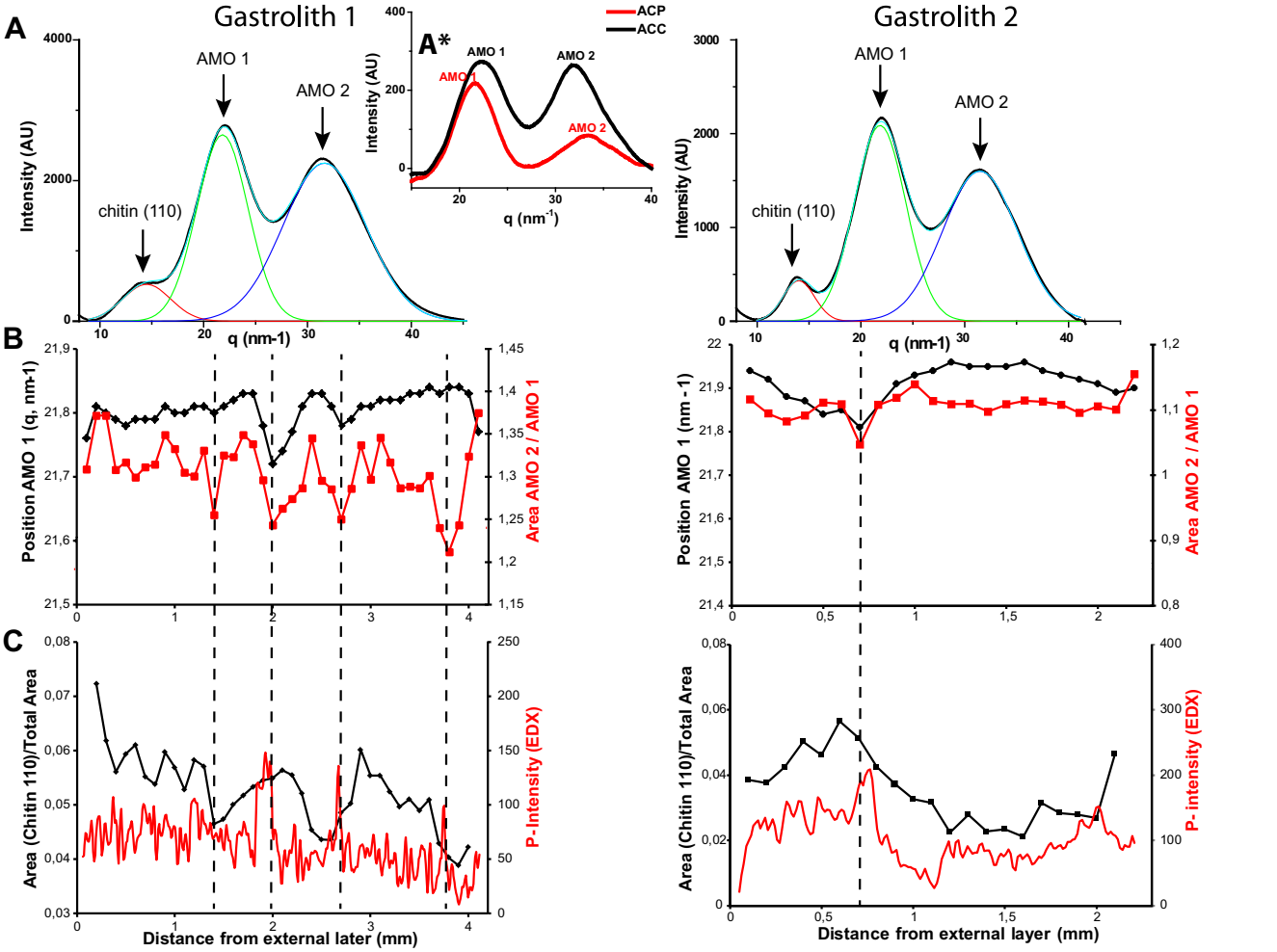


**Fig.7.** WAXS analysis on two cross-sections of embedded gastroliths showing, (A) the radially integrated WAXS pattern where the inset (A*) shows the XRD diffraction pattern of a synthetic ACC and ACP, (B) the position of AMO1 (black) and ratio between AMO2/AMO1 (red) as a function of the distance from the outermost external layer and (C) the corrected area of the chitin (1 1 0) signal and P-intensity as measured by EDS as a function of the distance from the outermost external layer. Dashed lines show the correlation between the P-rich regions in EDS and the decrease in AMO1 position and AMO2/AMO1 ratio in both samples. (For interpretation of the references to color in this figure legend, the reader is referred to the web version of this article.)

correspond to the GAMP-rich layers described in literature (Takagi et al., 2000), but possibly opens the well-discussed pathway of gastrolith proteins forming a link between the mineral and the chitin matrix and/or stabilizing the amorphous mineral (Glazer et al., 2010; Glazer and Sagi, 2012; Shechter et al., 2008b; Takagi et al., 2000; Yudkovski et al., 2010). Additionally, the described correlation between these proteins and the chitin scaffold could be an explanation for the observed increase in apparent chitin fiber size in SEM to 10–20 nm (Fig. 3E) in the earlier deposited inner layers, as well as the increase in protein content in Raman proceeding toward these layers (Fig. 6B).

## 5. Conclusion

By the use of spatially-resolved analysis we have shown that the crayfish gastrolith has a large variation in composition between different growth layers, reflecting changes in amounts of inorganic phosphate, protein content, chitin or small molecules like citrate or PEP. As everywhere in the gastrolith a stable amorphous mineral is present, the absence or presence of some of these additives in specific layers, in addition to the ACC bulk, indicates that there is not one but multiple strategies involved in stabilizing the gastrolithic ACC.

## Acknowledgments

We thank Stefan Siegel, Chenghao Li and prof. Oskar Paris for support during the SAXS + WAXS measurements at the μ-Spot beamline at BESSY II, Helmholtz-Zentrum Berlin, Ingrid Zenke for support with XRD measurements and Matthew A. Hood for editing the paper. We acknowledge financial support from the German Israeli Foundation (GIF), Research Grant No. 950-9.5/2007.

## References

Addadi, L., Raz, S., Weiner, S., 2003. Taking advantage of disorder: amorphous calcium carbonate and its roles in biomineralization. Adv. Mater. 15 (12), 959–970.

Aizenberg, J., Lambert, G., Addadi, L., Weiner, S., 1996. Stabilization of amorphous calcium carbonate by specialized macromolecules in biological and synthetic precipitates. Adv. Mater. 8, 222–226.

Akiva-Tal, A., Kababya, S., Balazs, Y.S., Glazer, L., Berman, A., Sagi, A., Schmidt, A., 2011. In situ molecular NMR picture of bioavailable calcium stabilized as amorphous $CaCO_3$ biomineral in crayfish gastroliths. Proc. Natl. Acad. Sci. U.S.A. 108, 14763–14768.

Beniash, E., Aizenberg, J., Addadi, L., Weiner, S., 1997. Amorphous calcium carbonate transforms into calcite during sea urchin larval spicule growth. Proc. R. Soc. London B 264, 461–465.

Bentov, S., Weil, S., Glazer, L., Sagi, A., Berman, A., 2010. Stabilization of amorphous calcium carbonate by phosphate rich organic matrix proteins and by single phosphoamino acids. J. Struct. Biol. 171, 207–215.

Bentov, S., Zaslansky, P., Al-Sawalmih, A., Masic, A., Fratzl, P., Sagi, A., Berman, A., Aichmayer, B., 2012. Enamel-like apatite crown covering amorphous mineral in a crayfish mandible. Nat. Commun. 3, 839.

De Gelder, J., De Gussem, K., Vandenabeele, P., Moens, L., 2007. Reference database of Raman spectra of biological molecules. J. Raman Spectrosc. 38, 1133–1147.

Glatter, O., Kratky, O., 1982. Small Angle X-ray Scattering. Academic Press Inc, London (pp. 35–36).

Glazer, L., Sagi, A., 2012. On the involvement of proteins in the assembly of the crayfish gastrolith extracellular matrix. Invert. Reprod. Dev. 56, 57–65.

Glazer, L., Schechter, A., Tom, M., Yudkovski, Y., Well, S., Aflalo, E.D., Pamuru, R.R., Khalaila, I., Bentov, S., Berman, A., Sagi, A., 2010. A protein involved in the assembly of an extracellular calcium storage matrix. J. Biol. Chem. 285, 12831–12839.

Huxley, T.H., 1880. The Crayfish. An Introduction to the Study of Zoology. Appleton and Company, New York.

Iconomidou, V.A., Chryssikos, G.D., Gionis, V., Willis, J.H., Hamodrakas, S.J., 2001. "Soft"-cuticle protein secondary structure as revealed by FT-Raman, ATR-FTIR and CD spectroscopy. Insect Biochem. Mol. Biol. 31 (9), 877–885.

Ihli, J., Kim, Y.-Y., Noel, E.H., Meldrum, F.C., 2013. The effect of additives on amorphous calcium carbonate (ACC): janus behavior in solution and the solid state. Adv. Funct. Mater. 23, 1575–1585.

Mahamid, J., Sharir, A., Gur, D., Zelzer, E., Addadi, L., Weiner, S., 2011. Bone mineralization proceeds through intracellular calcium phosphate loaded vesicles; a cryo-electron microscopy study. J. Struct. Biol. 174, 527–535.

Olszta, M.J., Cheng, X., Jee, S.S., Kumar, R., Kim, Y., Kaufman, M.J., Douglas, E.P., Gower, L.B., 2007. Bone structure and formation: a new perspective. Mater. Sci. Eng. R 58, 77–116.

Paris, O., Li, C., Siegel, S., Weseloh, G., Emmerling, F., Riesemeier, H., Erko, A., Fratzl, P., 2007. A new experimental station for simultaneous X-ray microbeam scanning for small- and wide-angle scattering and fluorescence at BESSY II. J. Appl. Crystallogr. 40, s466–s470.

Politi, Y., Arad, T., Klein, E., Weiner, S., Addadi, L., 2004. Sea urchin spine forms via a transient amorphous calcium carbonate phase. Science 306, 1161–1164.

Politi, Y., Batchelor, D.R., Zaslansky, P., Chmelka, B.F., Weaver, J., Sagi, I., Weiner, S., Addadi, L., 2010. Role of magnesium ion in the stabilization of biogenic amorphous calcium carbonate; a structure-function investigation. Chem. Mater. 22, 161–166.

Sato, A., Nagasaka, S., Furihata, K., Nagata, S., Arai, I., Saruwatari, K., Kogure, T., Sakuda, S., Nagasawa, H., 2011. Glycolitic intermediates induce amorphous calcium carbonate formation in crustaceans. Nat. Chem. Biol. 7, 197–199.

Sawada, K., 1997. The mechanisms of crystallization and transformation of calcium carbonates. Pure Appl. Chem. 69, 921–928.

Shechter, A., Berman, A., Singer, A., Freiman, A., Grinstein, M., Erez, J., Aflato, E.D., Sagi, A., 2008a. Reciprocal changes in calcification of the gastrolith and cuticle during the molt cycle of the red claw crayfish *Cherax quadricarinatus*. Biol. Bull. 214, 122–134.

Shechter, A., Glazer, L., Cheled, S., Mor, E., Weil, S., Berman, A., Bentov, S., Aflalo, E.D., Khalaila, I., Sagi, A., 2008b. A gastrolith protein serving a dual role in the formation of amorphous mineral containing extracellular matrix. Proc. Natl. Acad. Sci. U.S.A. 105, 7129–7134.

Takagi, Y., Ishii, K., Ozaki, N., Nagasawa, H., 2000. Immunolocalization of gastrolith matrix protein (GAMP) in the gastroliths and the exoskeleton of crayfish, *Procambarus clarkii*. Zoolog. Sci. 17, 179–184.

Termine, J.D., Peckauskas, R.A., Posner, A.S., 1970. Calcium phosphate formation in vitro II. Effects of environment on amorphous-crystalline transformation. Arch. Biochem. Biophys. 140, 318–328.

Travis, D.F., 1963. Structural features of mineralization from tissue to macromolecular levels of organization in the decapod crustacean. Ann. N. Y. Acad. Sci. 109, 177–245.

Yudkovski, Y., Glazer, L., Schechter, A., Reinhardt, R., Chalfa-Caspi, V., Sagi, A., Tom, M., 2010. Multi-transcript expression patterns in the gastrolith and the hypodermis of the crayfish *Cherax quadricarinatus* at premolt. Comp. Biochem. Physiol. D 5 (171–17).